Advances in Aircraft and Spacecraft Science, *Vol. 10, No. 1 (2023) 67-82*
https://doi.org/10.12989/aas.2023.10.1.067

Laboratory geometric calibration simulation analysis of push-broom satellite imaging sensor

Reza Sh. Hafshejani and Javad Haghshenas*

Department of Remote Sensing Payloads, Satellite System Research Institute, Iranian Space Research Center, Tehran, Iran

(Received July 5, 2022, Revised November 22, 2022, Accepted January 17, 2023)

Abstract. Linear array imaging sensors are widely used in remote sensing satellites. The final products of an imaging sensor can only be used when they are geometrically, radiometrically, and spectrally calibrated. Therefore, at the first stages of sensor design, a detailed calibration procedure must be carefully planned based on the accuracy requirements. In this paper, focusing on inherent optical distortion, a step-by-step procedure for laboratory geometric calibration of a typical push-broom satellite imaging sensor is simulated. The basis of this work is the simulation of a laboratory procedure in which a linear imager mounted on a rotary table captures images of a pin-hole pattern at different angles. By these images and their corresponding pinhole approximation, the correction function is extracted and applied to the raw images to give the corrected ones. The simulation results illustrate that using this approach, the nonlinear effects of distortion can be minimized and therefore the accuracy of the geometric position of this method on the image screen can be improved to better than the order of sub-pixel. On the other hand, the analyses can be used to proper laboratory facility selection based on the imaging sensor specifications and the accuracy.

Keywords: geometrical calibration; high resolution payload; laboratory calibration; optical distortion; remote sensing satellite

1. Introduction

Geometric calibration is one of the most important steps for optical remote sensing products. Since 1945, when the demand for precision cameras increased, the development of camera calibration methods has also progressed. Geometric calibration is usually in one of three forms: Plumb-Line Calibration, self-calibration, and on-the-job calibration (Lerma and Cabrelles 2007).

Various techniques have been developed for optical camera calibration which can be divided into two general categories. The first, are methods for directly measuring the optical distortion such as goniometer, multi-collimator base and stellar methods (Brown 1968, Clarke and Fryer 1998, Centre 2003). The second type is based on calculating parameters of the initially given mathematical calibration model such as projective invariant-based methods (plumb-line (Atkinson 1996, Clarke *et al.* 1998), cross-ratio (Li *et al.* 2014, Sun *et al.* 2016, Liao *et al.* 2019), vanishing points (Grammatikopoulos *et al.* 2007)) and targets resection (on-the-job calibration and self-calibration5 (Atkinson 1996)).

*Corresponding author, Ph.D., E-mail: j.haghshenas@isrc.ac.ir

http://www.techno-press.org/?journal=aas&subpage=7 ISSN: 2287-528X (Print), 2287-5271 (Online)

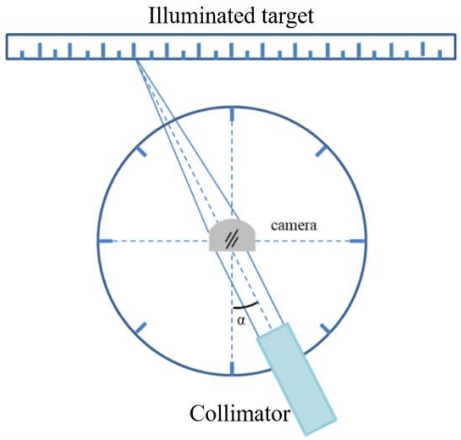

Fig. 1 Schematic of goniometer technique

Goniometer method: The goniometer technique includes placing a precise grid pattern (often referred to as a reseau plate) on the focal plane of the camera whereas backward illuminated (Fig. 1). Eventually, the angle between the image of the grid pattern were projected out into object space is measured in details (Hallert 1960).

Multi-collimator: In 1950, Washer *et al.* presented an arrangement of 25 collimators in 7.5-degree angular steps that provided acceptable values for distortion coefficients, focal length, resolution, prism effect, and principal point position (Washer and Case 1950). During those years, Carman was able to determine the position of the principal point and the focal length with an accuracy of 10 μm (Carman and Brown 1961).

Stellar calibration: This method uses the star specifications such as positions in Inertial coordinate system. The captured image (which contains hundreds of stars) will compare with standard star catalogues such as Hipparcos to extract the detailed geometric calibration matrix. The accuracy of this method is about several arcsecond but the processing time is too high and also the atmospheric effects must be considered in details (Schmid 1974).

Plumb-line: This method, which involves imaging parallel lines with detailed specified distances, is a suitable method for extracting distortion parameters. Setting up simplicity is one of the important advantages of this method in such a way that it does not require any high technology field equipment (Duane 1971). On the other hand, complicity of measuring the principal points offset from the center of the fiducial axes system is one of the important disadvantages of this method which leadings to a significant error in the estimation of the decentering distortion coefficients (Clarke *et al.* 1998).

Cross-ratio: Zhang proposed a method for calibrating the camera in 2003. He used cross-ratios technique for geometrical calibration of a camera system. The method was based on capturing a picture of a chessboard-pattern and selecting any collinear four points to calculate the two cross-ratios for object and image space, respectively. Their difference is attributed in distortion (Clarke *et al.* 1998). In later years, this method was improved by Ricolfe-Viala and Sánchez-Salmerón (2010).

Vanishing Points Method: This method is very simple to implement using the four corner points of a rectangular shape target which is lying in a common plane (Fig. 2). The image of these targets produces its perspective projection in image-space. In projective geometry, the view of rectangle

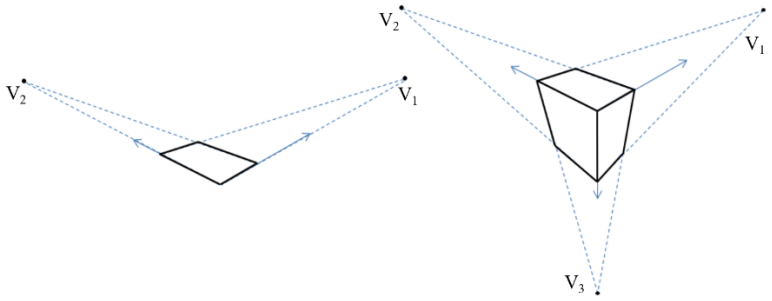

Fig. 2 Schematic of vanishing points

constitutes two vanishing points. Considering the origin in the projection center, these points define two perpendicular vectors in Euclidean coordinate system. So, their dot product has to be zero. It would be a conditional equation. Following this method guidelines, this setup could be established for more different views. This set of equations could be solved easily by least square method (Tan *et al.* 1995, Pajdla and Urban 1999).

Targets Resection methods (Self-calibration & on-the-job calibration), These methods use well-defined projective equations to calculate the deviation of the interior geometry of the camera from its ideal central projection (pinhole approximation). These equations, actually, define the straight transform relation between targets in object-space in a 3D cartesian coordinate system to the 2D image-space. Therefore, the calibration procedure in these methods, is based on tacking enough images of the target from different viewing angles (different setup geometry).

If the target's positions are accurately known in 3D cartesian coordinate system (using GPS or Theodolite), they are known as "Control Points". These kinds of targets will be used for "on-the-job" calibration. For "self-calibration" method, if the geometry configuration of the camera system is known accurately along with the additional calibration polynomial, there is even no need for a known 3D Cartesian coordinates of targets (Cramer 2004).

Linear array imaging (push-broom) payloads is widely used in remote sensing. The remote sensing payloads must undergo spectral, radiometric and geometric pre-launch and in-flight calibrations (Zhang *et al.* 2014, Tansock *et al.* 2015). Push-broom imaging has many benefits rather than other types of satellite imaging techniques, mostly due to the fact that each line of the image has its independent geometry and can be solved separately. Platform's low frequency vibration is also another source of error which geometrically affects an image (Haghshenas 2015, Haghshenas 2015, Haghshenas 2017).

Laboratory calibration of an infinite-focusing linear remote sensing (RS) cameras required an implementation of real-operating conditions in the laboratory, along with a proper mathematical model to acquire the calibration parameters.

In 2000 a calibration program was developed for the prototype model of the TLS (Three-Line Scanner) imaging system. This imaging system had three linear detectors for using push-broom imaging technique (based on laboratory calibration) (Chen *et al.* 2003); In the TLS project, the SMAC (Simultaneous Multi-frame Analytical Calibration) model developed by USGS was used (Woltring 1980, Merchanta *et al.* 2004). SMAC model procedure contains three main parts:1-principal points 2-radial distortion equation 3- decentering distortion equation. Different and more complicated models also developed based on SMAC model for TLS cameras which mostly used the auxiliary data from flight equipment (UAV or Satellites) which is beyond of the scope of this

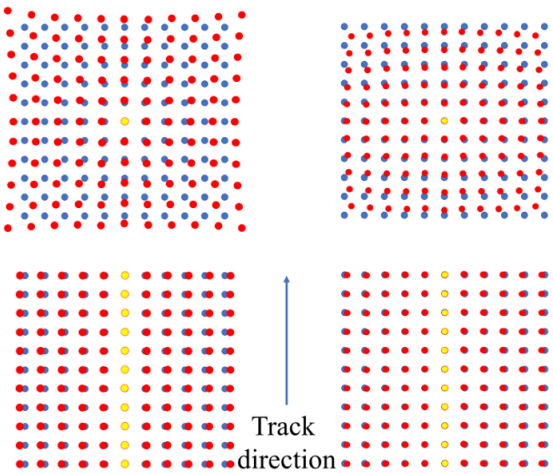

Fig. 3 Effect of radial distortion: (a) pin cushion distortion-frame camera (b) barrel distortion-frame camera (c) pin cushion distortion-linear array camera (d) barrel distortion-linear array camera

paper.

In this manuscript, we consider a linear detector which is installed at the focal plane array (FPA) of a high-resolution optic. Therefore, we must consider a laboratory calibration procedure which can be effective for extracting distortion coefficients, focal length, detector slope, and position of the principal point relative to the center of the detector with very high accuracy. As our detector array is linear type and the satellite imaging technique is push-broom, the laboratory setup includes: a high quality long focal length collimator (to simulate the image at infinity), a highly sensitive rotary table, a pinhole target and a calibrated light source. The payload under test, captures images of the pinhole at different angles of the field, which can be used to extract the parameters required for geometric calibration using a mathematical model.

2. Mathematical model of geometric calibration

2.1 Distorsion

Distortion is the only aberration that does not affect the image in terms of sharpness or focus. This aberration has the effect of creating a geometric nonlinear effect on the image coordinate plane. Distortion can be divided into three categories: Radial, Decentering, and Prism distortions (Hunt 1997).

• Radial Distortion: Radial distortion causes any image to be compressed or stretched by moving toward the edges of the field of view; In other words, each point of the image deviates from its ideal position (Bentley 2012). The effect of this type of distortion on a typical frame array imager and linear array imager is in the form of a cushion or barrel shown, (Fig. 3). In the (1), the coefficients k_1, k_2, and k_3 are related to this distortion.

$$\begin{cases}\Delta x_{RD} = x_{ip}\left(k_1 r_i^2 + k_2 r_i^4 + k_3 r_i^6\right) \\ \Delta y_{RD} = y_{ip}\left(k_1 r_i^2 + k_2 r_i^4 + k_3 r_i^6\right)\end{cases}$$

$$x_{ip} = x_p - x_i,$$
$$r_i = \sqrt{(x_p - x_i)^2 + (y_p - y_i)^2} \tag{1}$$

Where Δx_{RD} and Δy_{RD} are radial part of distortion and (x_p, y_p) is the position of principal point, and (x_{ip}, y_{ip}) is the position of point i with respect to principal point.

For cameras and projection systems, 2% distortion is an acceptable value (Walker 1994). But in photogrammetry, which requires high accuracy, 2% distortion will affect the results validity, and therefore distortion is an important issue which needs to be addressed correctly (Hunt 1997).

• Decentering distortion: This distortion is present in multi-lens systems and is due to the lack of alignment of the optical center of different system elements from manufacturing to the assembly phase (Fig. 4). Both radial and tangential terms are involved in distortion (Clarke *et al.* 1998). In the (2), the coefficients p1 and p2 are related to this distortion.

$$\begin{cases} \Delta x_{DD} = \left(2x_{ip}^2 + r_i^2\right)p_1 + 2x_{ip}y_{ip}p_2 \\ \Delta y_{DD} = \left(2y_{ip}^2 + r_i^2\right)p_2 + 2x_{ip}y_{ip}p_1 \end{cases} \tag{2}$$

Where Δx_{DD} and Δy_{DD} are decentering part of distortion.

• Thin prism distortion: The term comes from the fact that this aberration can be modelled by adding the mathematical model of a thin prism to the optical system (Clarke *et al.* 1998). This distortion originates from a small angle in the lens or sensor mounted on the focal plane (Duane 1971, Faig 1975, Wang *et al.* 2008). This distortion results from defective lens assembly or design, and like decentering distortion, occur in multiple lens systems (Weng *et al.* 1992). Both radial and tangential terms are involved in distortion too.

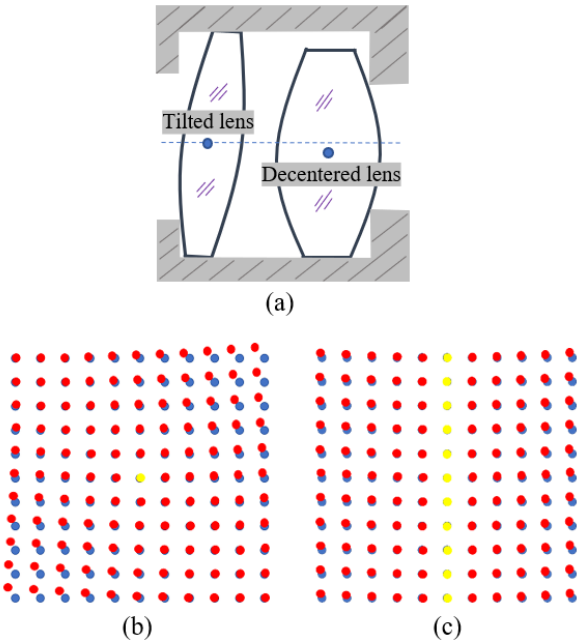

Fig. 4 (a) Lens decenter and lens tilt, (b) Tangential distortion- frame camera, and (c) Tangential distortion-linear array camera

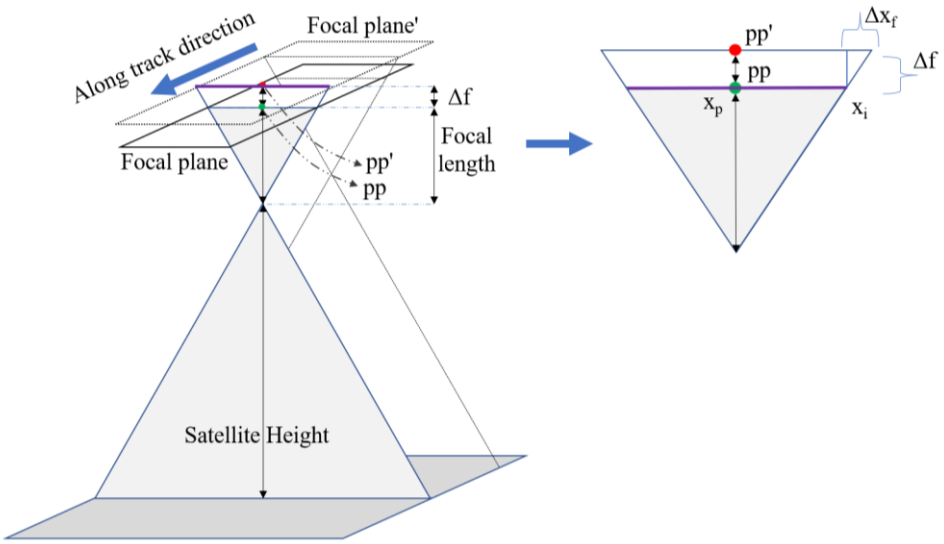

Fig. 5 Impact of a change in the camera constant on the x_i pixel position. Δf: changes in focal length. *pp*: principal point

Although radial, decentering, and thin prisms distortions can be formulated mathematically in an independent form, they are no longer independent in terms of physical properties (Wang *et al.* 2008). Radial and decentering distortions are the most effective systematic distortions in optical systems (Duane 1971), so in the following sections, the mathematical model of distortion resulting from radial and decentering terms will be described.

2.2 Principal point displacement and camera constant

In the perspective model, the camera is considered ideal. Hence the image center in this model is known as the principal point (pp). Usually due to an assembly error, the detector center is not located on the optical center and therefore the PP is drifted (Δx_{pp}, Δy_{pp}) (Atkinson 1996), (Fig. 5).

Camera constant is equal to the focal length of the camera in focus mode at infinity. If there is a change in the focal length camera constant along the detector line, it will affect the scale of the image coordinate axis, (Fig. 5). Using (4), the drift resulting from this scale change can be calculated (Atkinson 1996).

$$\frac{x_p - x_i}{f} = \frac{\Delta x_f}{\Delta f} \tag{3}$$

$$\Delta x_f = -(x_i - x_p)\frac{\Delta f}{f}\frac{x_p - x_i}{f} = \frac{\Delta x_f}{\Delta f} \tag{4}$$

2.3 Detector line angle

Detector lines is usually installed perpendicular to along-track direction in satellite imaging payloads, but may not be exactly perpendicular due to assembly errors. Hence, in the process of

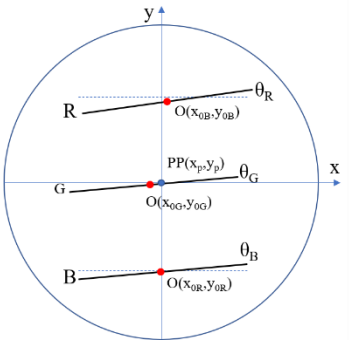

Fig. 6 Errors in the installation of the detector lines

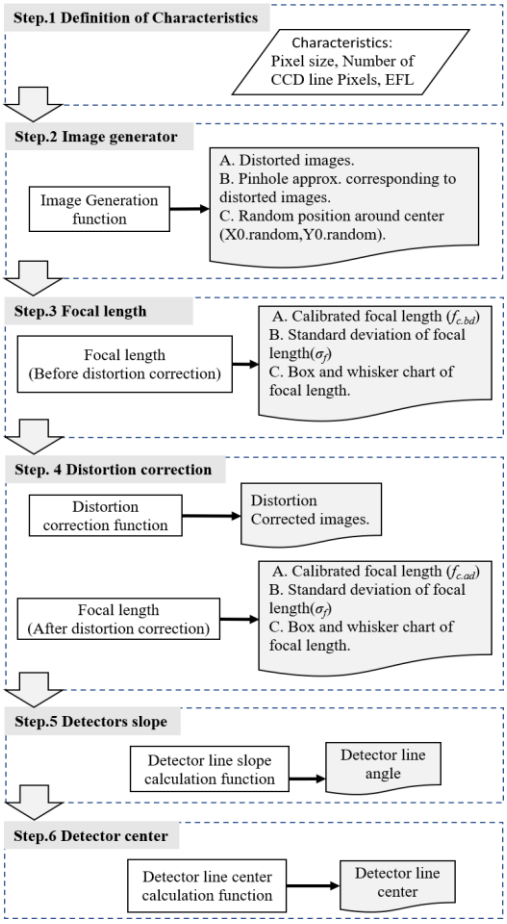

Fig. 7 Geometrical calibration simulation procedure

geometric calibration, the installation angle of each of them needs to be calculated with acceptable accuracy, (Fig. 6). The installation angle of detectors can be obtained by (6) for each pixel of line.

$$y_{ip} = P_1 x_{ip} + P_2 \tag{5}$$

$$\text{Detector angle} = P_1(\frac{180}{\pi}) \tag{6}$$

3. Geometric calibration simulation procedure

This method is designed to be used in the layout of a linear array camera geometric calibration test. The procedure for performing this simulation can be seen in the (Fig. 7).

3.1 Characteristics of imaging system

Detector line must be assembled in such a way that they are perpendicular to the along track direction, see (dash-line, Fig. 6). In practice, however, assembly problems cause errors in the system that change the distance between the detector lines, their installation angle, and ultimately their center position with respect to the optical point (solid-line, Fig. 6).

3.2 Image generator

In this step, three categories of data are produced as follow. Ideal images: perspective images of a pinhole pattern to be viewed by camera at $2N$+1 angle with steps of FOV/$2N$+1. Positions of the ideal images (x_n) are calculated by (7). In the (Fig. 8), x_{2N+1} shows the ideal position of the image obtained from the x_n equation. N represents number of images at each side of camera FOV.

$$x_n = f \times \tan\theta_n\,, \qquad n = 1, \dots, 2N+1 \tag{7}$$

Distorted images: Images that are simulated by applying the distortion function on ideal images (In the laboratory, these images can be captured by camera at $2N$+1 viewing angles.). In the (Fig. 9), x'_{2N+1} shows the distorted position of x_{2N+1} point.

Central images: The third category includes images that are used to extract the detector center. The images are taken at a zero angle in order to extract the distance between the detector center and the optics center on the detector plane. Since the rotating table has a positioning error, it is better to minimize this effect by averaging over several images (e.g., 8 images) taken at zero angle. Here, to simulate this error, the random function is applied to the ideal zero-angle image.

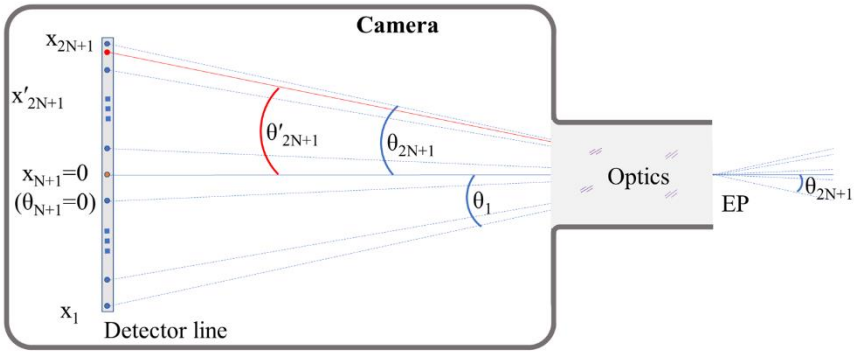

Fig. 8 Schematic of position of ideal images and distorted images on the detector. The detector image is exaggerated

3.3 Focal length

Due to optical system distortion, the focal length changes along a linear detector. Hence the focal length for each distorted point of image can be derived from the (8). Therefore, the calibrated focal length can be extracted by (9) (Washer and Case 1950). The standard deviation of the focal length (σ_f) is also calculated from the (10), where $\bar{f}$ refers to average of focal length of 91 images

$$f_n = \frac{x'_n}{\tan\theta_n} \tag{8}$$

$$f_c = f + \Delta f = f + \frac{\sum_{n=1}^{2N+1}|x_n - x'_n|}{\sum_{n=1}^{2N+1}|\tan\theta_n|} \tag{9}$$

$$\sigma_f = \sqrt{\frac{\sum_{n=1}^{2N+1}(f_n - \bar{f})^2}{N}} \tag{10}$$

3.4 Distortion correction

As mentioned, the various parameters of distortion (radial and decentering) are not physically separate. Therefore, the image distortion should be identified by solving the (11). This equation can be solved using linear regression.

$$\begin{cases} \Delta x = \Delta x_{RD} + \Delta x_{DD} \\ \Delta y = \Delta y_{RD} + \Delta y_{DD} \end{cases} \tag{11}$$

3.5 Detector slope

To extract the installation angle of detector, it is enough to fit a line on the position of each pinhole image by linear regression, (6). If N=20, then 41 images are taken at different angles of the field of view. Therefore, there are 41 locations that can be used to calculate the installation slope of the detector, (Fig. 9).

3.6 Detector center position

Position of central images that are taken in step.2 should be averaged using (12), and (13), to

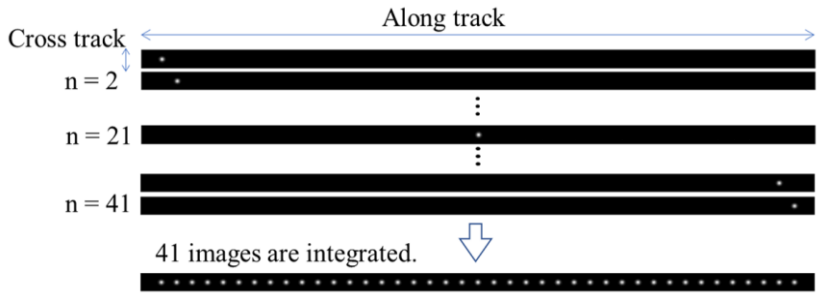

Fig. 9 Schematic of simulated images

Table 1 Parameter used in simulation

Parameters	Value
Satellite altitude	550 km
EFL	1000 mm
Detector size	78 mm
Swath	50.5 km
FOV	5.26 deg
(Pixel size, GSD, IFOV)	(5.5 μm, 3.5 m, 1.3 arcsec) (7 μm, 4.5 m, 1.7 arcsec) (8.75 μm, 5.5 m, 2.1 arcsec) (10.7 μm, 7 m, 2.6 arcsec) (12 μm, 7.5 m, 2.9 arcsec)
Distortion Coefficients	k_1=6.51E-06 k_2=-9.23E-10 k_3=5.88E-14 p_1=-3.62E-08 p_2=-7.79E-09

calculate the detector center drift of principal point (0, 0).

$$x_c = \frac{\sum_{i=1}^{M}(x_{i,\max})}{M} \tag{12}$$

$$y_c = \frac{\sum_{i=1}^{M}(y_{i,\max})}{M} \tag{13}$$

Where the point (x_c, y_c) is the position of the detector center with respect to principal point position, (0, 0). Also point ($x_{i,\max}$, $y_{i,\max}$) refer to position of maximum value of each image ,and M refer to number of captured images.

4. Analysis and discussions

In this section, the accuracy of this methodology is discussed carefully. Therefore, affecting factors are investigated here. Simulations are done for a remote sensing payload with the specifications presented in (Table 1). Different typical pixel sizes are considered in simulations for trend analysis. IFOV refers to instantaneous field of view, GSD refers to ground sampling distance, and EFL refers to effective focal length.

4.1 Focal length

Using the data of (Table 1) and N=45, 91 images were simulated and by the process mentioned in Fig. 7, the calibration process was followed. The calibrated focal length (f_c) was changed from 1004.21 mm (before calibration) to 1000.02 mm (after calibration), which is much closer to the paraxial focal length (1000 mm).

With this method, the standard deviation of the focal length (σf) has decreased from 3.733

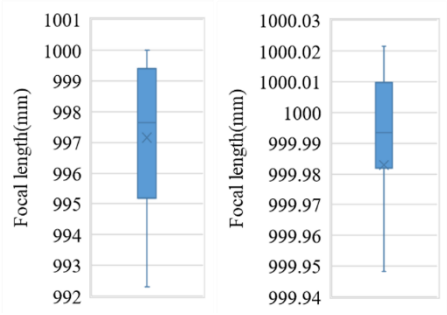

(a) (b)

Fig. 10 Box and whisker chart of focal length: (a) Before geometric calibration. (b) After geometric calibration

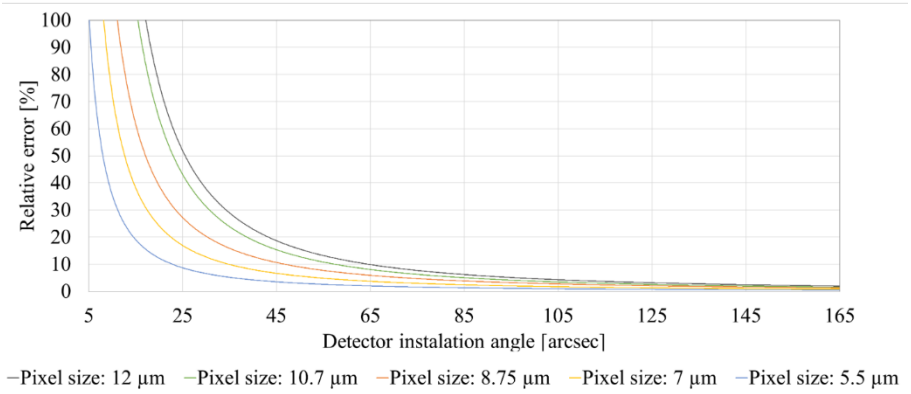

Fig. 11 Accuracy of detector angle

(before calibration) to 0.02 (after calibration). (Fig. 10) illustrates the box and whisker chart of focal length.

4.2 Detector installation angle

We have considered both relative error (*RE*) and absolute error (*AE*) as a measure of accuracy for more effecting analysis and providing a better understanding of the subject. Here, absolute error stands for *AE*=|true value-calculated value| and relative error stands for REaccuracy= (*AE*/True value)×100.

Using (Table 1), (Fig. 11) illustrates the *RE* in different angles. Smaller the pixel size, smaller the RE. The RE is less than 10% for all pixel sizes and angles greater than 65 arcsec. On the other hand, it is less than 5% for installation angles greater than 100 arcsec. (Fig. 11) could be used as a look-up figure guideline for designer in the first few steps to estimate the proper parameters of the system.

Fig. 12 illustrates *AE* for a typical CCD installation angle, 90 arcsec. Dotted-line in this figure, illustrate the IFOV corresponding to each pixel size for 1000 mm EFL. We can conclude, increasing pixel size will increase the absolute error but it will remain in IFOV limitation range.

Along and cross track root mean square (RMS) error of the calibrated images are illustrated in

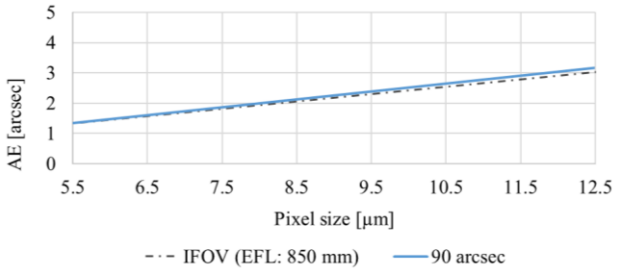

Fig. 12 Absolute error of detector angle vs. pixel size

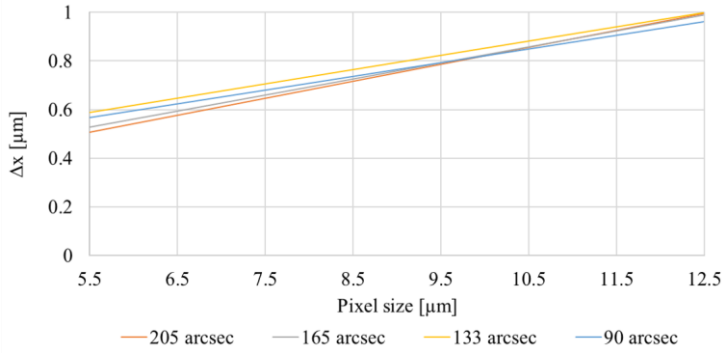

Fig. 13 Deviation of distortion corrected image of ideal image in cross-track direction (Δx)

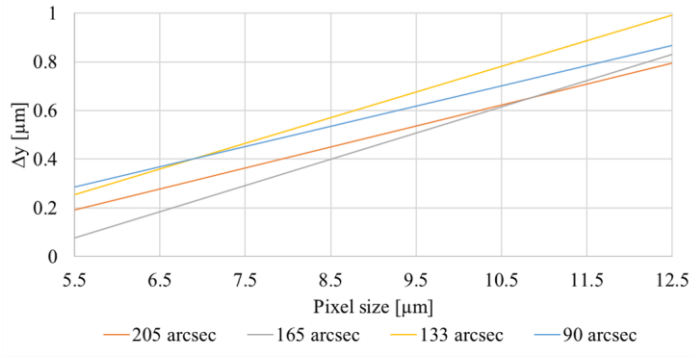

Fig. 14 Deviation of distortion corrected image and ideal image in along-track direction (Δy)

(Fig. 13) and (Fig. 14), respectively. We can confirm that the RMS error is less than 1µm in both directions.

4.3 Positioning accuracy of rotating table

The accuracy of the rotating table positioning is an important factor which can restricts this method performance. On the other hand, a very high-performance rotary may be over-qualified and will add the extra cost to the system. To avoid overdesigning of the instrument specifications, effects of rotary table accuracy on the final performance of this geometrical calibration

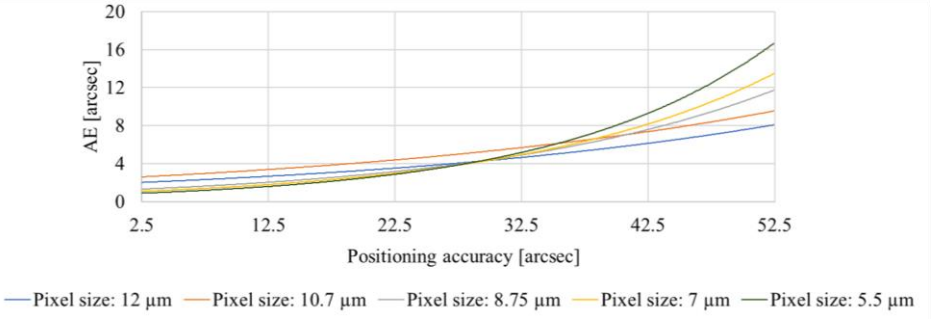

Fig. 15 Rotation table positioning accuracy

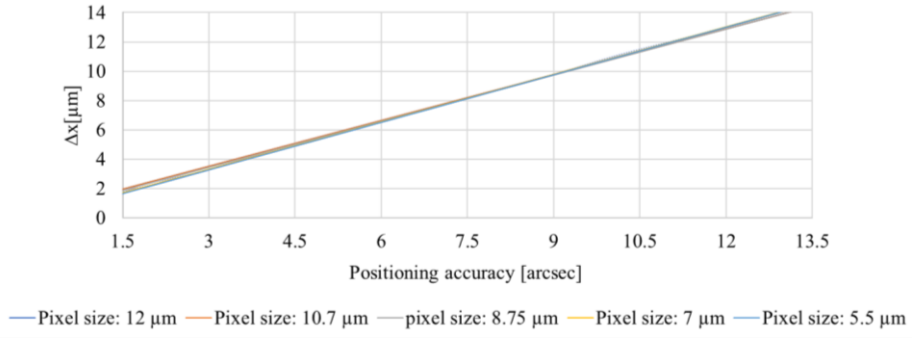

Fig. 16 RMS of distortion corrected image deviation of ideal position (Δx)

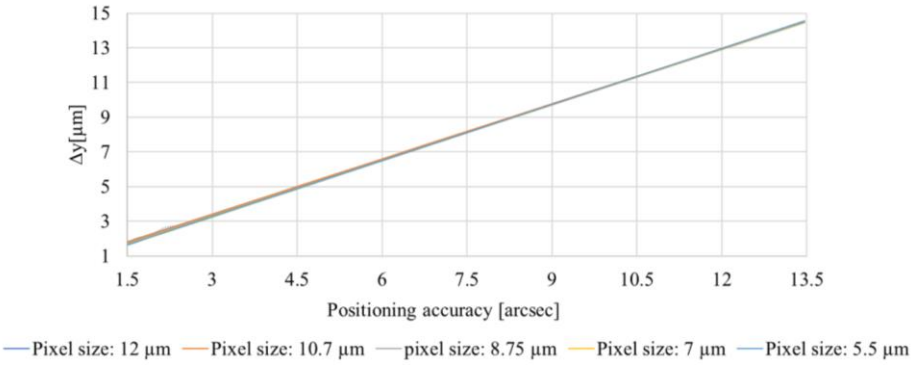

Fig. 17 RMS of distortion corrected image deviation of ideal position (Δy)

methodology is investigated in this section.

Fig. 15 illustrates AE for a range of rotary table positioning accuracy. (Fig. 16) and (Fig. 17) illustrate the deviation of the calibrated image from original ideal image in along track (Δx) and cross-track (Δy), respectively. Using these graph results we can conclude that RMS error of distortion corrected image deviation of ideal position (Δx, Δy) is smaller than the pixel size.

Results of (Fig. 15), (Fig. 16), and (Fig. 17) shows that final performance is very sensitive to the rotating table positioning accuracy. Doubling the positioning accuracy will roughly double the method accuracy. Another conclusion comes from (Fig. 15) is that the sensitivity behaviour is

Table 2 Parameter used in simulation

Name	x0.Ideal	x0.cal	Y0.Ideal	Y0.ph.cal
Detector center	0 μm	8 μm	0 μm	5 μm

linear somewhere, in our case in 27.5 arcsec, and will exponentially increase for lower performance rotary table. Therefore, for a system with specific pixel size and its corresponding IFOV, along with the accuracy requirement budget, this result can be used as a useful guideline for optimized rotating table selections.

4.4 Center position of detectors

Eight images were taken at a zero angle (nadir viewing). The maximum of each of these images was calculated and then the average position of these points was calculated according to (8), and (9). As can be seen from the data in (Table 2), the calculated values of the center of each detector line differ by less than a pixel from the expected value.

5. Conclusions

This manuscript presents an applicable easy-to-implement methodology for geometric calibration of linear cameras. The presented method, which is based on capturing images of a pinhole pattern using a defined instruments setup was designed to be simply implemented in the laboratory for remote sensing earth observation satellite cameras.

We have discussed the accuracy limitations of this approach and the more affecting parameters are analysed separately. Our results show that using this approach can guarantee the sub-pixel accuracy for a typical push-broom payload geometry calibration.

On the other hands, the instrument setup and its requirements are discussed properly to help the researchers do it easily by themselves and avoid extra costs. Furthermore, another advantage of this method is speeding up the testing duration and also it would be simplifying and speed up the calculation and analysis process.

References

Atkinson, K.B. (1996), *Close Range Photogrammetry and Machine Vision*, Whittles.

Bentley, J. (2012), "Field guide to lens design, spie field guides vol", FG27, Bellingham, WA, USA.

Brown, D.C. (1968), "Advanced methods for the calibration of metric cameras", DBA SYSTEMS INC MELBOURNE FL.

Carman, P. and Brown, H. (1961), "Camera calibration in Canada", *Can. Survey.*, **15**(8), 425-439.

Centre, O.M. (2003), *Handbook of Practical Camera Calibration Methods and Models Optical Metrology Centre*, Chapter 4, Camera Calibration Methods.

Chen, T., Shibasaki, R. and Shunji, M. (2003), "Development and calibration of the airborne three-line scanner (TLS) imaging system", *Photogram. Eng. Remote Sens.*, **69**(1), 71-78. https://doi.org/10.14358/PERS.69.1.71.

Clarke, T., Wang, X. and Fryer, J. (1998), "The principal point and CCD cameras", *Photogramm. Record*, **16**(92), 293-312. https://doi.org/10.1111/0031-868X.00127.

Clarke, T.A. and Fryer, J.G. (1998), "The development of camera calibration methods and models", *Photogramm. Record*, **16**(91), 51-66. https://doi.org/10.1111/0031-868X.00113.

Cramer, M. (2004), "EuroSDR network on digital camera calibration", *Report Phase*, **1**, 53S.

Duane, C.B. (1971), "Close-range camera calibration", *Photogramm. Eng*., **37**(8), 855-866.

Faig, W. (1975), "Calibration of close-range photogrammetric systems: Mathematical formulation", Univ. New Brunswick, Fredericton, N.B., Canada.

Grammatikopoulos, L., Karras, G. and Petsa, E. (2007), "An automatic approach for camera calibration from vanishing points", *ISPRS J. Photogram. Remote Sens.*, **62**(1), 64-76. https://doi.org/10.1016/j.isprsjprs.2007.02.002.

Haghshenas, J. (2015), "Effects of satellite platform's vibrations on the image quality of a remote sensing payload: system level design and challenges", *Optical Systems Design 2015: Optical Design and Engineering VI, International Society for Optics and Photonics*.

Haghshenas, J. (2015), "Maximum allowable low-frequency platform vibrations in high resolution satellite missions: challenges and look-up figures", *Optical Systems Design 2015: Optical Design and Engineering VI, International Society for Optics and Photonics*.

Haghshenas, J. (2017), "Vibration effects on remote sensing satellite images", *Adv. Aircraft Spacecraft Sci.*, **4**(5), 543. https://doi.org/10.12989/aas.2017.4.5.543.

Hallert, B. (1960), *Photogrammetry, Basic Principles and General Survey*, McGraw-Hill.

Hunt, C.L. (1997), "Automatic calibration of a video camera lens system", Master of Technology in Information Engineering at Massey University, Massey University.

Lerma, J.L. and Cabrelles, M. (2007), "A review and analyses of plumb-line calibration", *Photogram. Record*, **22**(118), 135-150. https://doi.org/10.1111/j.1477-9730.2007.00412.x.

Li, D., Wen, G., Hui, B.W., Qiu, S. and Wang, W. (2014), "Cross-ratio invariant based line scan camera geometric calibration with static linear data", *Opt. Laser. Eng.*, **62**, 119-125. https://doi.org/10.1016/j.optlaseng.2014.03.004.

Liao, R., Zhu, J., Yang, L., Lin, J., Sun, B. and Yang, J. (2019), "Flexible calibration method for line-scan cameras using a stereo target with hollow stripes", *Opt. Laser. Eng.*, **113**, 6-13. https://doi.org/10.1016/j.optlaseng.2018.09.014.

Merchanta, D., Schenka, A., Habibb, A. and Yoona, T. (2004), "USGS/OSU progress with digital camera in situ calibration methods", *Post-launch calibration of satellite sensors: Proceedings of the International Workshop on Radiometric and Geometric Calibration*, Gulfport, Mississippi, December.

Pajdla, T. and Urban, M. (1999), "Camera calibration from bundles of parallel lines".

Ricolfe-Viala, C. and Sánchez-Salmerón, A.J. (2010), "Correcting non-linear lens distortion in cameras without using a model", *Opt. Laser Technol.*, **42**(4), 628-639. https://doi.org/10.1016/j.optlastec.2009.11.002.

Schmid, H. (1974), "Stellar calibration of the orbigon lens", *Photogram. Eng.*, **40**(1), 101-111.

Sun, B., Zhu, J., Yang, L., Yang, S. and Niu, Z. (2016), "Calibration of line-scan cameras for precision measurement", *Appl. Opt.*, **55**(25), 6836-6843. https://doi.org/10.1364/AO.55.006836.

Tan, T., Sullivan, G.D. and Baker, K.D. (1995), *Recovery of Intrinsic and Extrinsic Camera Parameters using Perspective Views of Rectangles*, BMVC, Citeseer.

Tansock, J., Bancroft, D., Butler, J., Cao, C., Datla, R., Hansen, S., Helder, D., Kacker, R., Latvakoski, H. and Mylnczak, M. (2015), "Guidelines for radiometric calibration of electro-optical instruments for remote sensing", National Institute of Standards and Technology.

Walker, R.E. (1994), *Marine Light Field Statistics*, Wiley-Interscience.

Wang, J., Shi, F., Zhang, J. and Liu, Y. (2008), "A new calibration model of camera lens distortion", *Pattern Recogn.*, **41**(2), 607-615. https://doi.org/10.1016/j.patcog.2007.06.012.

Washer, F.E. and Case, F.A. (1950), "Calibration of precision airplane mapping cameras", *Photogram. Eng.*, **16**(4), 502-524.

Weng, J., Cohen, P. and Herniou, M. (1992), "Camera calibration with distortion models and accuracy evaluation", *IEEE Trans. Pattern Anal. Mach. Intel.*, **14**(10), 965-980.

Woltring, H. (1980), "Simultaneous multiframe analytical calibrations (SMAC) by recourse to oblique

observations of planar control distributions", *NATO Symposium on Applications of Human Biostereometrics, International Society for Optics and Photonics*.

Zhang, G., Jiang, Y., Li, D., Huang, W., Pan, H., Tang, X. and Zhu, X. (2014), "In-orbit geometric calibration and validation of ZY-3 linear array sensors", *Photogram. Record*, **29**(145), 68-88. https://doi.org/10.1111/phor.12052.

EC